Secondary instabilities in the collisionless Rayleigh-Taylor instability: Full kinetic simulation

Takayuki Umeda and Yasutaka Wada

Articles you may be interested in

Plasma kinetic effects on interfacial mix
Physics of Plasmas **23**, 112302112302 (2016); 10.1063/1.4966562

Self-induced longitudinal current in the perpendicular ion cyclotron heating in a tokamak
Physics of Plasmas **23**, 112501112501 (2016); 10.1063/1.4966563

Fluid theory and kinetic simulation of two-dimensional electrostatic streaming instabilities in electron-ion plasmas
Physics of Plasmas **23**, 112110112110 (2016); 10.1063/1.4967283

Theory based scaling of edge turbulence and implications for the scrape-off layer width
Physics of Plasmas **23**, 112502112502 (2016); 10.1063/1.4966564

Secondary instabilities in the collisionless Rayleigh-Taylor instability: Full kinetic simulation

Takayuki Umeda[a)] and Yasutaka Wada
Institute for Space-Earth Environmental Research, Nagoya University, Nagoya 464-8601, Japan

The nonlinear evolution of the Rayleigh-Taylor instability (RTI) at a density shear layer transverse to magnetic field in collisionless plasma is investigated by means of a fully kinetic Vlasov simulation with two spatial and two velocity dimensions. The primary RTI in the MHD regime develops symmetrically in a coordinate axis parallel to gravity as seen in the previous MHD simulations. Small-scale secondary instabilities are generated due to secondary velocity shear layers formed by the nonlinear development of the primary RTI. The secondary instabilities take place asymmetrically in the coordinate axis parallel to gravity. It is suggested that these secondary instabilities correspond to the electron Kelvin-Helmholtz instability generated by the electron velocity shear, whose development depends on the polarity of the inner product between the magnetic field and the vorticity of the velocity shear layer. *Published by AIP Publishing.*
[http://dx.doi.org/10.1063/1.4967859]

I. INTRODUCTION

The Rayleigh-Taylor instability (RTI) is a well-known hydrodynamic instability in neutral fluid as well as in magnetized plasma, which grows at an interface between two fluids when a light fluid supports a heavy fluid against an external force such as gravity. It has been known from (neutral) hydrodynamic simulations that the interface develops as rising bubbles of the light fluid between falling spikes (known as finger/mushroom structures) of the heavy fluid. The magneto-hydro-dynamic (MHD) simulations have shown that the development of the RTI transverse to the ambient magnetic field in collisionless magnetized plasmas is similar to that in the neutral fluid.[1–3] The primary RTI takes place in various situations in natural plasma, such as in the atmosphere/ionosphere of stars/planets due to gravity. The RTI is also generated as a secondary instability of the Kelvin-Helmholtz instability (KHI) due to a centrifugal force.[4,5]

Numerical simulations for the RTI with non-MHD effect have been performed by using the Hall MHD code,[6–9] the Finite-Larmor-Radius (FLR) MHD code,[8–10] and the hybrid particle-in-cell (PIC) code.[11,12] In contrast to these previous studies, we perform a full kinetic simulation by using a Vlasov code, which may be one of the first attempts for a full kinetic simulation study of the RTI. The previous studies focused on non-MHD effects to the development of the primary RTI, while we focus on *secondary* instabilities at non-MHD scales in the present study.

During the nonlinear evolution of the RTI, various secondary instabilities such as RTI and KHI are induced by a velocity shear and a density shear at secondary interfaces between the light and heavy fluids.[2,3,6,7] Even when the primary RTI is at the MHD scale, smaller-scale structures generated by secondary processes of the RTI are sometimes at non-MHD scales. The purpose of the present study is to examine particle kinetic effects on the secondary processes by performing a full kinetic simulation.

II. VLASOV SIMULATION SETUP

The Vlasov code used in the present study solves the Vlasov equation (1) together with the Maxwell equations (2) in two spatial and two velocity dimensions (x, y, v_x, v_y), which has already been used for the studies of the KHI[13,14]

$$\frac{\partial f}{\partial t} + \boldsymbol{v} \cdot \frac{\partial f}{\partial \boldsymbol{x}} + \frac{q}{m}(\boldsymbol{E} + \boldsymbol{v} \times \boldsymbol{B}) \cdot \frac{\partial f}{\partial \boldsymbol{v}} = 0, \tag{1}$$

$$\left.\begin{array}{c} \dfrac{1}{c^2}\dfrac{\partial \boldsymbol{E}}{\partial t} - \nabla \times \boldsymbol{B} + \mu_0 \boldsymbol{J} = 0 \\[6pt] \dfrac{\partial \boldsymbol{B}}{\partial t} + \nabla \times \boldsymbol{E} = 0 \\[6pt] \nabla \cdot \boldsymbol{E} - \dfrac{\rho}{\epsilon_0} = 0 \\[6pt] \nabla \cdot \boldsymbol{B} = 0 \end{array}\right\}. \tag{2}$$

The code adopts a non-oscillatory and conservative semi-Lagrangian scheme[15,16] with several improvements[17,18] for solving the Vlasov equation (1), which exactly satisfies the continuity equation for charge

$$\frac{\partial \rho}{\partial t} + \nabla \cdot \boldsymbol{J} = 0. \tag{3}$$

The Maxwell equations are solved with the standard Finite-Difference-Time-Domain (FDTD) method[19] as in PIC simulations. The code is well parallelized and is made a performance tuning for recent supercomputers.[20] The detailed descriptions of the simulation code are given in the references.

In the previous (extended-)MHD simulations,[7–10] the initial density shear layer was in the state of the one-dimensional MHD equilibrium. The previous hybrid PIC simulations used a discontinuous density layer with a step function, which is not in an equilibrium state.[11,12] In the

a)Email: taka.umeda@nagoya-u.jp

present study, we perform a Vlasov simulation of a long simulation time on several hundreds of ion gyro period with a time step on electron plasma period. Hence, it is important to use a "stable" initial condition in order to maintain the initial density shear layer for a long simulation time. As an initial condition for the present study, we derive a new equilibrium which satisfies one-dimensional time-independent (steady-state) two-fluid equations for ions and electrons.

Let us consider a four-dimensional phase space with two spatial and two velocity dimensions (x, y, v_x, v_y) and the gravity in the y direction. In the present coordinate system, the out-of-plane electric field E_z component and the in-plane magnetic field B_x and B_y components are not considered since the out-of-plane current J_z component does not exist. Here, we consider a one-dimensional equilibrium for a density shear layer in which all the physical quantities depend only on the y coordinate. Then, the time-independent two-fluid equations for ions and electrons are written as follows:

$$\frac{\partial P_e}{\partial y} - eN_e(B_z U_{xe} + E_y) = m_e N_e g_y, \tag{4}$$

$$\frac{\partial P_i}{\partial y} + eN_i(B_z U_{xi} + E_y) = m_i N_i g_y, \tag{5}$$

$$\frac{\partial E_y}{\partial y} = \frac{e}{\epsilon_0}(N_i - N_e), \tag{6}$$

$$\frac{\partial B_z}{\partial y} = e\mu_0(N_i U_{xi} - N_e U_{xe}), \tag{7}$$

where U_x represents the bulk velocity of fluids in the x direction.

We derive a two-fluid equilibrium with the following assumptions: $N_i = N_e (\equiv N)$, $\partial \beta_{i,e}/\partial y = 0$ (where $\beta_{i,e} = 2\mu_0 P_{i,e}/B_z^2 = 2\omega_{pi,e}^2 V_{ti,e}^2/(c^2\omega_{ci,e}^2)$ with V_t being the thermal velocity), and

$$N[y] = \frac{N_I - N_{II}}{2}\tanh\left[\frac{y}{L}\right] + \frac{N_I + N_{II}}{2}, \tag{8}$$

where L represents the half thickness of the density shear layer. The subscripts I and II represent the upper and lower boundaries, respectively. By solving P, B_z, and U_x, we obtain

$$P_s[y] = \frac{(m_e + m_i)\beta_s g_y}{\beta_i + \beta_e + 1}\left\{\frac{N_I - N_{II}}{2}\log\left[e^{\frac{y}{L}} + e^{-\frac{y}{L}}\right] + \frac{N_I + N_{II}}{2}y\right\} + P_{0s}, \tag{9}$$

$$B_z[y] = \sqrt{\frac{2\mu_0 P_i[y]}{\beta_i}} = \sqrt{\frac{2\mu_0 P_e[y]}{\beta_e}}, \tag{10}$$

$$U_{xi}[y] = \frac{g_y}{eB_z[y]}\left\{m_i - \frac{(m_e + m_i)\beta_i}{\beta_i + \beta_e + 1}\right\}, \tag{11}$$

$$U_{xe}[y] = -\frac{g_y}{eB_z[y]}\left\{m_e - \frac{(m_e + m_i)\beta_e}{\beta_i + \beta_e + 1}\right\}. \tag{12}$$

Here, P_0 is an integral constant which is determined such that the pressure corresponds to P_I at the upper boundary.

In the present study, we assume that $N_I/N_{II} = 9$, $\beta_i = \beta_e = 0.125$, and $g_y = -0.000063\omega_{pi}V_{ti}$. The half thickness of the initial density shear is set as $L = 4d_i = 12r_i$ at $y = 0$, where d_i and r_i are the ion inertial length and the ion thermal gyro radius, respectively. The simulation system is taken for $0 \leq x \leq 3L$ and $-6L \leq y \leq 6L$ with $N_x \times N_y = 400 \times 1600$ grid points. Thus, the grid spacing in the configuration space is $\Delta = 0.0075L = 4\lambda_{Di,I}$ for both x and y directions. The velocity space is taken for $-20V_t \leq v_{x,y} \leq 20V_t$ for both ions and electrons, with $N_{vx} \times N_{vy} = 100 \times 100$ grid points. Thus, the grid spacing in the velocity space is $\Delta v_{i,e} = 0.4V_{ti,e}$. The time step is $\Delta t = 0.025/\omega_{pe,I}$. It should be noted that we adopt a reduced ion-to-electron mass ratio $m_i/m_e = 25$ for computational efficiency.

The initial spatial profiles of N, B_z, $P = (P_i + P_e)$, and $U_{xi,e}$ as functions of y are shown in Fig. 1. Here, $B_{zI} = \sqrt{2\mu_0 P_{sI}/\beta_s}$. The initial velocity distributions of the ions and electrons for the Vlasov simulation are isotropic Maxwellian with the bulk (drift) velocity $U_{xi,e}[y]$ and the thermal velocity $V_{ti,e}[y] \equiv \sqrt{P_{i,e}[y]/mN[y]}$. Therefore, the initial condition is not a Vlasov equilibrium.

The initial bulk velocity of the MHD fluid U_x in the previous (extended-)MHD simulations[7–10] was assumed to be zero since the MHD equilibrium can take an arbitrary bulk velocity for density shear layers. On the other hand, the initial bulk velocity of ions and electrons in full kinetic simulations is non-zero due to the $\boldsymbol{g} \times \boldsymbol{B}$ drift and the diamagnetic drift. It is noted that the initial bulk velocity of ions in the previous hybrid simulations[11,12] was neglected because of the step-like sharp gradient of the density shear layer at the spatial grid scale.

In contrast to PIC simulations where instabilities grow from thermal noises/fluctuations due to a finite number of particles, Vlasov simulations need a seed perturbation to initiate instabilities as fluid simulations do. Most of the previous (extended-)MHD simulations imposed multiple wave modes with random phase as an initial perturbation, while we impose a single wave mode as an initial perturbation. This is because our interests are in physical processes rather than natural phenomena. Turbulent mixing of multiple RT modes in the nonlinear evolution sometimes makes it difficult to identify secondary instabilities and their generation mechanisms. The initial perturbation in the present study has the following form:

$$\delta U_{yi,e}[x, y] = U_0 \frac{\cos[k_x x]}{\cosh^2\left[\frac{y}{L}\right]}, \tag{13}$$

with $U_0 = 0.01B_{zI}/\sqrt{\mu_0 m_i N_I}$ and $k_x = 2\pi/(3L)$ (mode 1). Since the wavelength of the primary RT mode is $\lambda_{RT} = 3L = 12d_i = 48r_i$ at $y = 0$, the primary RTI is in the MHD regime.

III. SIMULATION RESULT

Figure 2 shows the spatial profiles of ion density at different times. The RTI develops symmetrically in a coordinate axis parallel to gravity ($t\omega_0 = 4$ and 6 where $\omega_0 \equiv \sqrt{g_y/L} \sim \omega_{cil}/23$), and typical bubble and finger/mushroom structures are formed as seen in the previous
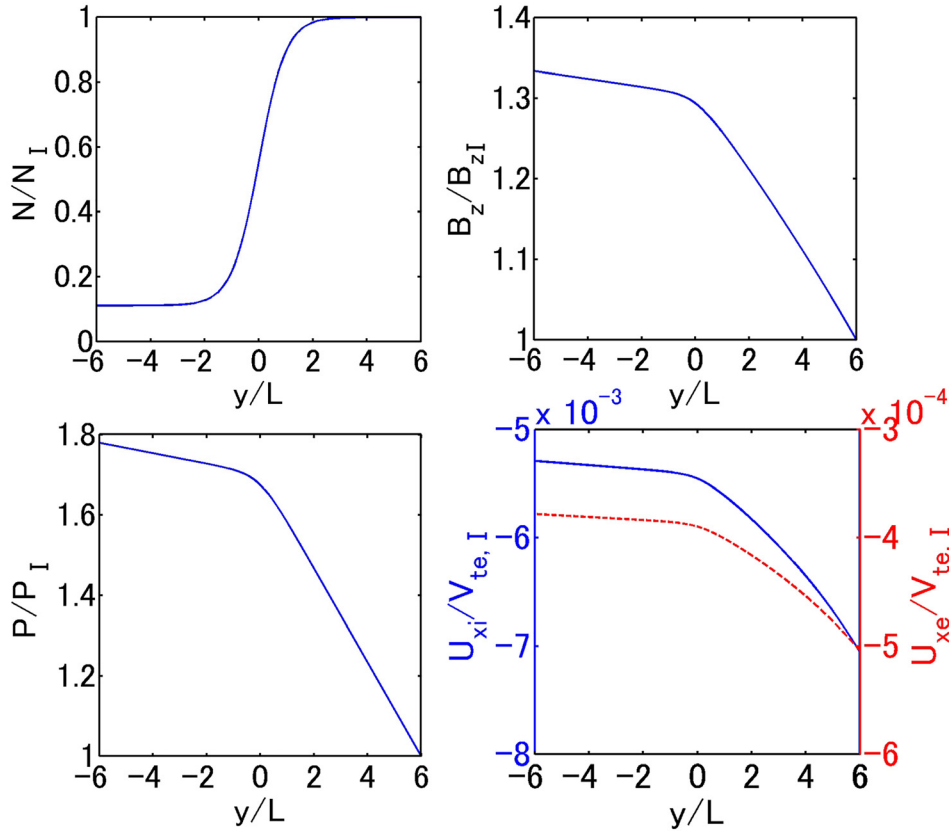
FIG. 1. Initial spatial profiles of the density N, the magnetic field B_z, the scalar pressure $P = (P_i + P_e)$, and the bulk velocity $U_{xi,e}$ as functions of y.

MHD simulations. A secondary instability is generated at the right-hand side of the finger/mushroom structure at $t\omega_0 = 6.5$. Other secondary instabilities are also generated at the upper edge of the bubble at $t\omega_0 = 6.9$. These instabilities develop asymmetrically in a coordinate axis parallel to gravity. The secondary instability at the right-hand side develops faster than at the left-hand side as seen at $t\omega_0 = 7.2$ and 7.7.

During the development of the primary RTI, "secondary density/velocity shear layers" are formed along the edge of the bubble and mushroom structures. The thickness of the secondary shear layers is narrower than that of the primary shear layer, which becomes a source of smaller-scale secondary instabilities. In order to analyze the generation mechanism of

secondary instabilities, we focus on the structure and thickness of the secondary shear layers.

A. Tip of finger

Figure 3 shows the structure of the secondary shear layer at the lower-edge (tip) of the finger/mushroom structure at $t\omega_0 = 5.8$. As shown in the two-dimensional spatial profile of the ion density in panel (a), we define the coordinate axes ξ and ζ as the directions normal and tangential to the density shear layer, respectively. The panels (b), (c), (d), and (e) show the one-dimensional spatial profile in the normal (ξ) direction of the density $N_{i,e}$, the magnetic field B_z, the scalar
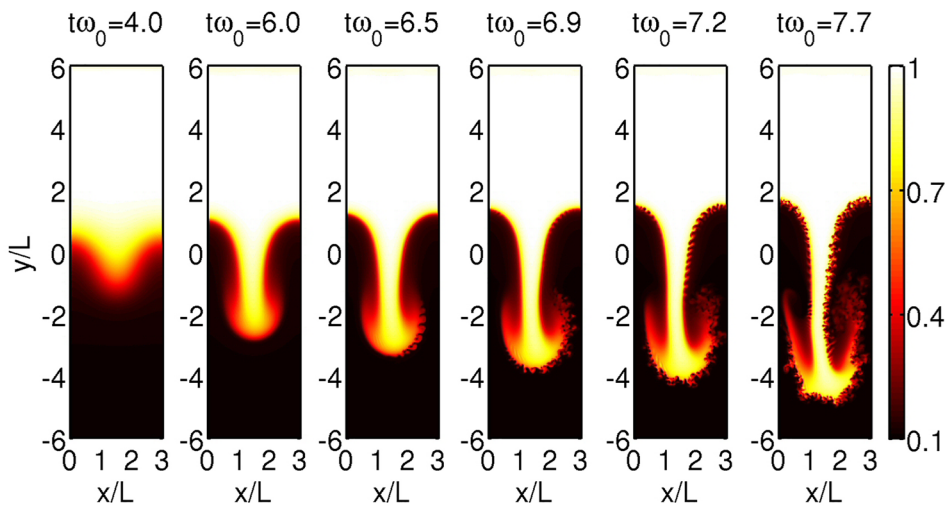

FIG. 2. Spatial profiles of ion density at different times.

pressure $P_{i,e}$, and the tangential bulk velocity $U_{\zeta i,e}$, respectively. The left and right panels of (b–e) show the profiles at the left- and right-hand side of the bottom of the finger/mushroom structure, respectively.

At both of shear layers, the ion and electron densities in panel (b) have almost the same profiles. The magnetic field in panel (c) has a local minimum at both of the shear layers. A secondary instability takes place at the local minimum of the magnetic field at the right-hand side of the tip of the finger/mushroom structure ($\xi = 0$), while there is no secondary instability at the left-hand side.

The wavelength of the secondary instability at the right-hand side of the tip of the finger is $\lambda_{2nd} = 0.26L$. There are various candidates of the secondary instability, such as the current-sheet kink instability (CSKI), the lower-hybrid drift instability (LHDI), and the electron-scale Kelvin-Helmholtz instability (EKHI). The CSKI is generated by an electric current across magnetic fields and its typical wavelength is estimated as $\lambda_{CSK} \sim 2\pi\sqrt{d_i d_e}$.[21] The LHDI is generated by a relative drift between ions and electrons across magnetic fields and its typical wavelength is estimated as $\lambda_{LHD} \sim 2\pi\sqrt{r_i r_e}$.[22] The EKHI is generated by an electron velocity shear and its typical wavelength is estimated as $\lambda_{EKH} \sim 4\pi L_{Ue}$, where L_{Ue} represents the half thickness of an electron velocity shear layer.[23]

We estimate d_i, d_e, r_i, and r_e at the secondary shear layer from the cross-section profiles along the normal direction ξ shown in Fig. 3. We also estimate L_{Ue} by fitting a $\tanh(\xi/L_{Ue})$ function to the electron bulk velocity. The wavelengths of the CSKI, LHDI, and EKHI with the parameters at the right-hand side of the tip of the finger/mushroom structure are obtained as $\lambda_{CKS} \sim 0.98L$, $\lambda_{LHD} \sim 0.21L$, and $\lambda_{EKH} \sim 0.26L$, respectively. The wavelengths of the secondary instability at the right-hand side are close to those of the LHDI and the EKHI. However, the secondary instability is generated at the local minimum of the magnetic field, where the relative velocity between ions and electrons (i.e., electric current) is zero. Hence, it is suggested that the secondary instability at the right-hand side of the tip of the finger/mushroom structure corresponds to the EKHI.

A previous study on the secondary instabilities in the primary KHI[14] suggested that the stability of secondary shear layers depends on the polarity of $\mathbf{B} \cdot \mathbf{\Omega}_2$, where $\mathbf{\Omega}_2 = \nabla \times \mathbf{U}_{i2}$ is the vorticity of the secondary velocity shear of ions. The electron velocity shear ($\partial U_{\zeta,e}/\partial\xi$) at the right-hand side of the tip of the finger is about ten times stronger than that at the left-hand side. The polarity of $\mathbf{B} \cdot \mathbf{\Omega}_2$ is positive at the right-hand side but is negative at the left-hand side, which is consistent with the previous study.[14]

Below, we discuss the reasons for the asymmetry of the velocity shear. We found that the velocities of both ion and electron bulk are expressed by the sum of the $\mathbf{E} \times \mathbf{B}$ drift, the diamagnetic drift, and the $\mathbf{g} \times \mathbf{B}$ drift, i.e.

$$U_s = \frac{\mathbf{E} \times \mathbf{B}}{|B|^2} - \frac{(\nabla \cdot \mathbf{P}_s) \times \mathbf{B}}{q_s N_s |B|^2} + \frac{m_s \mathbf{g} \times \mathbf{B}}{q_s |B|^2}, \tag{14}$$

where $\mathbf{P}_s$ represents the pressure tensor for the species s, and $q_i = -q_e = e$. It is note that the stress tensor in the electron
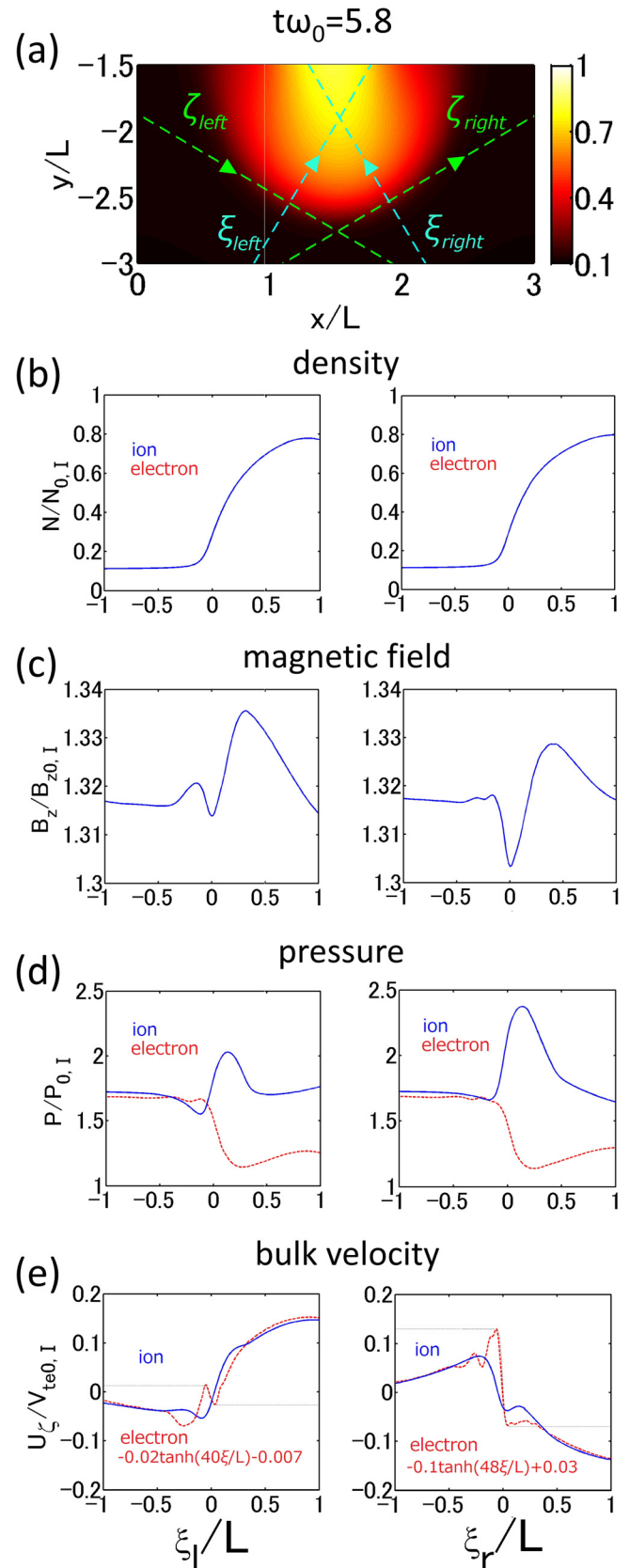

FIG. 3. Structure of the secondary shear layer at the lower-edge (tip) of the finger/mushroom structure at $t\omega_0 = 5.8$. Two-dimensional spatial profile of the ion density together with the definition of the coordinate axes taken in the directions normal and tangential to the density shear layer (a). One-dimensional spatial profile in the normal (ξ) direction of the density $N_{i,e}$ (b), the magnetic field B_z (c), the scalar pressure $P_{i,e}$ (d), and the tangential bulk velocity $U_{\zeta i,e}$ (e).

pressure is very small ($\mathbf{P}_e \simeq P_e\mathbf{I}$ where $\mathbf{I}$ is the unit tensor), suggesting that the electron gyro-kinetics is negligible. It is also noted that the contribution of the $\mathbf{g} \times \mathbf{B}$ drift is smaller than the other two drifts. We also found that the electric field is expressed by the sum of the MHD term, the Hall term, and the pressure gradient term, i.e.

$$\mathbf{E} = -\mathbf{U}_i \times \mathbf{B} + \frac{\mathbf{J} \times \mathbf{B}}{eN} - \frac{\nabla P_e}{eN}. \quad (15)$$

Note that the Ampere law ($\mu_0\mathbf{J} = \nabla \times \mathbf{B}$) is well satisfied.

As seen in panel (e) of Fig. 3, the ion bulk velocity has a step-like (tanh type) form at MHD spatial scale with several substructures at ion spatial scale. The MHD-scale structure of the ion bulk velocity has the different polarity of $\partial U/\partial \xi$ from the left-hand side to the right-hand side, which consists of the $\mathbf{E} \times \mathbf{B}$ drift. The ion-scale substructure of the ion bulk velocity has (almost) a unipolar ($1/\cosh^2$ type) form with the same polarity at both sides. The difference between the bulk velocities of ions and electrons comes from the Hall term, since $\mathbf{U}_e = \mathbf{U}_i - \mathbf{J}/(eN)$. Since the $\mathbf{E} \times \mathbf{B}$ drift does not

generate any electric current, the diamagnetic current is dominant in the total current, $\mathbf{J} \simeq (\nabla \cdot \mathbf{P}) \times \mathbf{B}/|\mathbf{B}|^2$, where $\mathbf{P} = \mathbf{P}_i + P_e\mathbf{I}$ with a symmetric P_e.

In Figure 4, we show the structure of the electric current at the tip of the finger. Panel (a) shows the contour lines of the magnetic field B_z at $t\omega_0 = 5.8$, which indicate the structures of the electric current loops. The arrows show the direction of the current, the dashed lines show the coordinate axis ξ in Fig. 3, and the cross marks show $\xi = 0$. Panels (b) and (c) show the one-dimensional spatial profiles of the current density components in the tangential direction at the left-hand side (b) and the right-hand side (c) of the tip of the finger, respectively. The total current J_ζ shown by the dotted lines consists of the MHD component of the ion diamagnetic current shown by the solid lines, i.e., $J_{\zeta,i,\mathrm{MHD}} = (\nabla P_i \times \mathbf{B})_\zeta/|\mathbf{B}|^2$, the non-MHD component of the ion diamagnetic current, shown by the circles, i.e., $J_{\zeta,i,\mathrm{non-MHD}} = (\nabla \cdot \mathbf{\Pi}_i \times \mathbf{B})_\zeta/|\mathbf{B}|^2$ (where $\mathbf{P}_i = P_i\mathbf{I} + \mathbf{\Pi}_i$), and the electron diamagnetic current shown by dashed lines, i.e., $J_{\zeta,e} = (\nabla P_e \times \mathbf{B})_\zeta/|\mathbf{B}|^2$.

The total (diamagnetic) current at the left-hand side and the right-hand side has a bipolar form with the same polarity, turning from positive to negative. However, the amplitude of the total current at the right-hand side is larger than that at the left-hand side. The electron diamagnetic current has (almost) a unipolar form with the opposite polarity to the total current. From panels (b) and (c) of Fig. 4, it is expected that the MHD component of the ion diamagnetic current is dominant. It is obvious from Fig. 3 that the asymmetry of the MHD component of the ion diamagnetic current between the right-hand side and the left-hand side is due to the gradient of the ion scalar pressure. We expect that the asymmetry of the ion scalar pressure results from non-MHD terms depending on the polarity of $\mathbf{B} \cdot \mathbf{\Omega}$.

B. Base of finger

Figure 5 shows the structure of the secondary shear layer at the upper-edge of the bubble (base of the finger) structure at $t\omega_0 = 6.4$ with the same format as Fig. 3. At the shear layers at both of left-hand side and right-hand side of the base of the finger, the ion and electron densities in panel (b) have almost the same profiles. The magnetic field in panel (c) has a local maximum at both of the shear layers. Secondary instabilities take place at the local maximum of the magnetic field at both sides of the base of the finger structure ($\xi = 0$).

The wavelengths of the secondary instabilities at the left-hand side and the right-hand side of the base of the finger are $\lambda_{2nd} = 0.19L$ and $0.2L$, respectively. In a similar way to the Subsection III A, we estimate d_i, d_e, r_i, and r_e of the secondary shear layer from the cross-section profiles along the normal direction ξ shown in Fig. 5. We also estimate L_{Ue} by fitting a $\tanh(\xi/L_{Ue})$ function to the electron bulk velocity. The wavelengths of the CSKI, LHDI, and EKHI with the parameters at the left-hand side of the base of the finger structure are obtained as $\lambda_{CKS} \sim 0.89L$, $\lambda_{LHD} \sim 0.2L$, and $\lambda_{EKH} \sim 0.19L$, respectively. The wavelengths of the CSKI, LHDI, and EKHI with the parameters at the right-hand side are also obtained as $\lambda_{CKS} \sim 0.88L$, $\lambda_{LHD} \sim 0.21L$, and
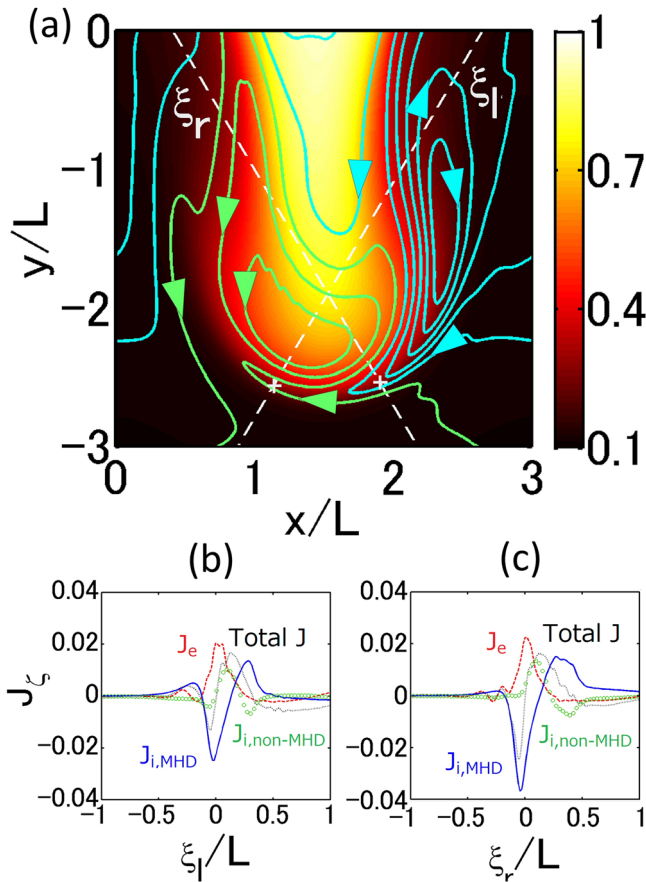

FIG. 4. Contour lines of the magnetic field B_z together with the ion density at $t\omega_0 = 5.8$ (a), and the corresponding one-dimensional spatial profiles of the current density components in the tangential direction at the left-hand side (b) and the right-hand-side (c) of the tip of the finger structure. The arrows and dashed lines in panel (a) indicate the direction of the current and the coordinate axis ξ in Fig. 3 with the cross marks being $\xi = 0$. The solid lines, the circles, the dotted lines, and the dashed lines in panels (b) and (c) represent the MHD component of the ion diamagnetic current, the non-MHD component of the ion diamagnetic current, the total current, and the electron diamagnetic current, respectively.
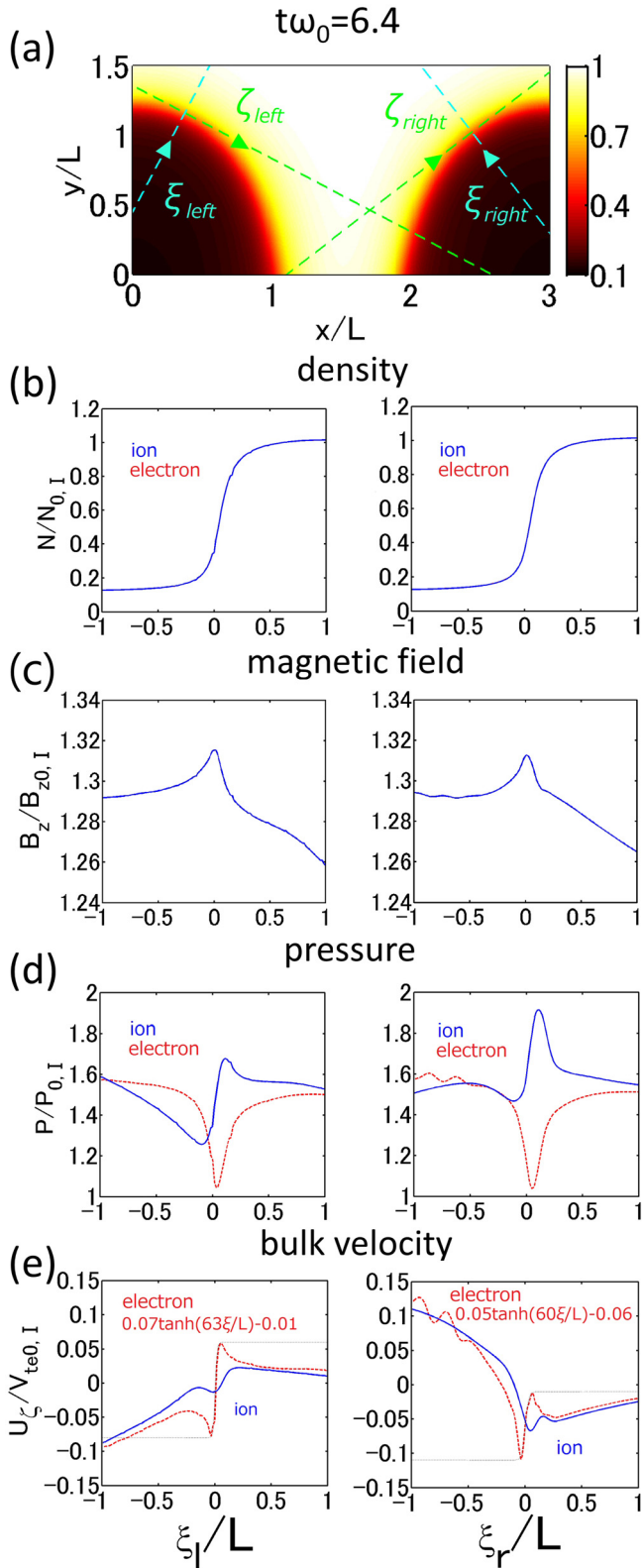
FIG. 5. Structure of the secondary shear layer at the upper-edge of the bubble (base of the finger) structure at $t\omega_0 = 6.4$ with the same format as Fig. 3.

$\lambda_{EKH} \sim 0.2L$, respectively. The wavelengths of the secondary instabilities at both sides of the base of the finger are close to that of the LHDI and the EKHI. However, the secondary instabilities are generated at the local maximum of the magnetic field, where the relative velocity between ions

and electrons (i.e., electric current) is zero. Hence, it is suggested that the secondary instabilities at both sides of the base of the finger structure correspond to the EKHI.

In contrast to the tip of the finger, the secondary instabilities are generated at both sides of the base of the finger, although the polarity of $\boldsymbol{B} \cdot \boldsymbol{\Omega}_2$ is positive at the right-hand side of the finger but is negative at the left-hand side. The spatial profiles of the ion and electron bulk velocities at the left-hand side and the right-hand side of the base of the finger are different from each other as seen in panel (e) of Fig. 5, while the electron shear (i.e., magnitude of $\partial U_\zeta / \partial \xi$) at both sides is almost same. This is why the secondary instabilities are generated simultaneously at both sides.

The velocities of both ion and electron bulk are expressed by the sum of the $\boldsymbol{E} \times \boldsymbol{B}$ drift, the diamagnetic drift, and the $\boldsymbol{g} \times \boldsymbol{B}$ drift as at the tip of the finger. As seen in panel (e) of Fig. 5, the ion bulk velocity at the right-hand side of the base of the finger has a step-like (tanh type) form at MHD spatial scale with $\partial U_\zeta / \partial \xi < 0$. On the other hand, the ion bulk velocity at the left-hand side has a ramp-like form at MHD spatial scale with $\partial U_\zeta / \partial \xi > 0$. The MHD-scale structure of the ion bulk velocity consists of the $\boldsymbol{E} \times \boldsymbol{B}$ drift with different polarity of $\partial \boldsymbol{U} / \partial \xi$ from the left-hand side to the right-hand side. As described in the Subsection III A, the difference between the bulk velocities of ions and electrons comes from the (total) diamagnetic current. It is expected from panel (c) of Fig. 5 that the diamagnetic
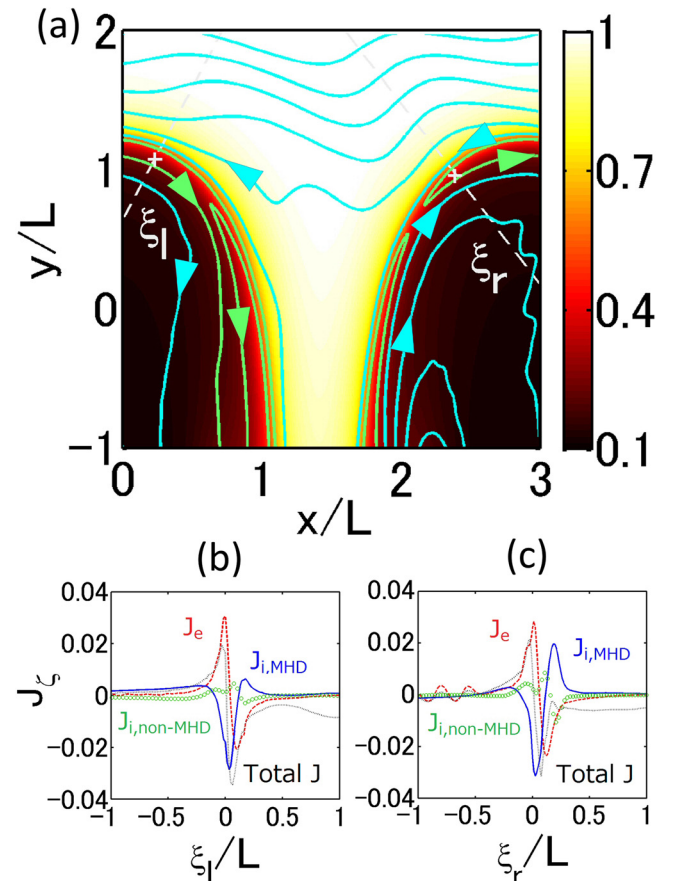

FIG. 6. Structure of the electric current at $t\omega_0 = 6.4$ with the same format as Fig. 4.

current has a bipolar form with the same polarity at both sides of the base of the finger.

In Figure 6, we show the structure of the electric current at $t\omega_0 = 6.4$ and at the base of the finger with the same format as Fig. 4. In contrast to the tip of the finger, the structures of the total current at the left-hand side and the right-hand side are similar to each other, with almost the same amplitude. From panels (b) and (c) of Fig. 6, it is expected that the electron diamagnetic current is dominant. As at the tip of the finger, there is asymmetry between the structure of the MHD and non-MHD component of the ion diamagnetic current at the left-hand side and the right-hand side of the base of the finger. However, the asymmetry of the MHD and non-MHD component cancels each other out.

As seen in panel (a) of Fig. 6, the structure of the electric current is generally asymmetric in the coordinate axis parallel to gravity. Since the structure of the electric current in the tangential direction is (unexpectedly) symmetric between the onset points, the secondary instabilities at the base of the finger are generated simultaneously. However, there is asymmetry between the development of the secondary instabilities between the left-hand side and the right-hand side of the base of the finger. The secondary instability at the right-hand side of the finger develops faster than the secondary instability at the left-hand side as shown in Fig. 2. Since the polarity of $\boldsymbol{B} \cdot \boldsymbol{\Omega}_2$ is negative at the left-hand side, the development of the secondary instability is suppressed. Since the polarity of $\boldsymbol{B} \cdot \boldsymbol{\Omega}_2$ is positive at the right-hand side, on the other hand, the secondary instability develops along the edge of the finger. These results are consistent with those of the previous study on the secondary instability of the KHI.[14]

IV. CONCLUSION AND DISCUSSION

A four-dimensional (two spatial dimensions and two velocity dimensions) Vlasov simulation is performed to study the non-MHD effects on the nonlinear processes of the RTI. In the previous MHD simulations, secondary (Kelvin-Helmholtz) instabilities are generated symmetrically in a coordinate axis parallel to gravity at both sides of the finger/mushroom structure. By contrast, secondary instabilities at kinetic spatial scale are generated asymmetrically at the tip and base of the finger in the present full kinetic simulation.

It is confirmed that the generation and the development of secondary instabilities taking place at the secondary shear layers of the RT fingers/bubbles is affected by the orientation of the magnetic field and the vorticity of the velocity field at the secondary shear layers ($\boldsymbol{B} \cdot \boldsymbol{\Omega}_2$). A secondary instability develops when $\boldsymbol{B} \cdot \boldsymbol{\Omega}_2$ is positive but does not really develop when $\boldsymbol{B} \cdot \boldsymbol{\Omega}_2$ is negative, which is consistent with the previous study on the KHI.[14] The secondary instability develops at local extrema (maximum or minimum) of the magnetic field, where the electric current is zero, but there exists a strong electron velocity shear. It is suggested from our analysis that the secondary instability corresponds to the electron-scale KHI, which is described by the electron-MHD equations.[23] The present secondary instability was not seen in the previous extended-MHD and hybrid simulations since the temporal development of the electron bulk velocity was

not solved explicitly. Detailed linear analysis on the competition between the electron KHI and other instabilities such as a LHDI is left as a future study.

We suggest the following scenario for the asymmetric development of the secondary instability at the primary RTI. The ion scalar pressure develops asymmetrically between the left-hand side and the right-hand side of the leading edge of the finger and bubble structures depending on the polarity of $\boldsymbol{B} \cdot \boldsymbol{\Omega}_2$. The asymmetric ion pressure generates an asymmetric diamagnetic current and then an asymmetric Hall electric field. Then, the structure of the electron bulk velocity becomes asymmetric due to the $\boldsymbol{E} \times \boldsymbol{B}$ drift, which results in a strong velocity shear at a velocity shear layer with $\boldsymbol{B} \cdot \boldsymbol{\Omega}_2 > 0$.

Finally, we discuss the asymmetry of the scalar pressure. The time development of the ion scalar pressure with the stress term is described as follows in the present coordinate system:

$$\frac{\partial P_i}{\partial t} = -(\boldsymbol{U}_i \cdot \nabla)P_i - 2P_i(\nabla \cdot \boldsymbol{U}_i) - (\boldsymbol{\Pi}_i \nabla) \cdot \boldsymbol{U}_i - \frac{\nabla \cdot \boldsymbol{Q}_i}{2}, \tag{16}$$

where $(\boldsymbol{\Pi}_i \nabla)$ represents a matrix product and $\boldsymbol{Q}_i \equiv (Q_{xxxi} + Q_{xyyi}, Q_{xxyi} + Q_{yyyi})$ represents a heat flux vector. It has been shown by our previous study[24] that the stress tensor $\boldsymbol{\Pi}_i$ can be roughly approximated by the gyro viscosity.[25] Then, the stress term in Eq. (16) becomes zero, which suggests that the asymmetric development of the scalar pressure is affected by the heat flux. The detailed analysis of such higher moments is left as a future study.

[1]Y.-M. Wang and M. Nepveu, Astron. Astrophys. **118**, 267–274 (1983), see http://adsabs.harvard.edu/abs/1983A%26A...118..267W.

[2]B.-I. Jun, M. L. Norman, and J. M. Stone, Astrophys. J. **453**, 332–349 (1995).

[3]J. M. Stone and T. Gardiner, Phys. Fluids **19**, 094104 (2007).

[4]Y. Matsumoto and M. Hoshino, Geophys. Res. Lett. **31**, L02807, doi:10.1029/2003GL018195 (2004).

[5]Y. Matsumoto and M. Hoshino, J. Geophys. Res. **111**, A05213, doi:10.1029/2004JA010988 (2006).

[6]B. Srinivasan and X.-Z. Tang, Phys. Plasmas **19**, 082703 (2012).

[7]J. D. Huba, J. G. Lyon, and A. B. Hassam, Phys. Rev. Lett. **59**, 2971–2974 (1987).

[8]R. Goto, H. Miura, A. Ito, M. Sato, and T. Hatori, Plasma Fusion Res. **9**, 1403076 (2014).

[9]R. Goto, H. Miura, A. Ito, M. Sato, and T. Hatori, Phys. Plasmas **22**, 032115 (2015).

[10]J. D. Huba, Phys. Plasmas **3**, 2523–2532 (1996).

[11]D. Winske, Phys. Plasmas **3**, 3966–3974 (1996).

[12]J. D. Huba and D. Winske, Phys. Plasmas **5**, 2305–2316 (1998).

[13]T. Umeda, J. Miwa, Y. Matsumoto, T. K. M. Nakamura, K. Togano, K. Fukazawa, and I. Shinohara, Phys. Plasmas **17**, 052311 (2010).

[14]T. Umeda, S. Ueno, and T. K. M. Nakamura, Plasma Phys. Controlled Fusion **56**, 075006 (2014).

[15]T. Umeda, Earth, Planets Space **60**, 773–779 (2008).

[16]T. Umeda, Y. Nariyuki, and D. Kariya, Comput. Phys. Commun. **183**, 1094–1100 (2012).

[17]H. Schmitz and R. Grauer, Comput. Phys. Commun. **175**, 86–92 (2006).

[18]T. Umeda, K. Togano, and T. Ogino, Comput. Phys. Commun. **180**, 365–374 (2009).

[19]K. S. Yee, IEEE Trans. Antennas Propag. **14**, 302–307 (1966).

[20]T. Umeda, K. Fukazawa, Y. Nariyuki, and T. Ogino, IEEE Trans. Plasma Sci. **40**, 1421–1428 (2012).

[21]H. Suzuki, M. Fujimoto, and I. Shinohara, Adv. Space Res. **30**, 2663–2666 (2002).

[22]W. Daughton, Phys. Plasmas **10**, 3103–3119 (2003).

[23]G. Gaur and A. Das, Phys. Plasmas **19**, 072103 (2012).

[24]T. Umeda, N. Yamauchi, Y. Wada, and S. Ueno, Phys. Plasmas **23**, 054506 (2016).

[25]W. B. Thompson, Rep. Prog. Phys. **24**, 363–424 (1961).